PHYSICAL REVIEW E **99**, 013110 (2019)

Characterizing the impact of particle behavior at fracture intersections in three-dimensional discrete fracture networks

Thomas Sherman,[1,2,3] Jeffrey D. Hyman,[1,*] Diogo Bolster,[3] Nataliia Makedonska,[1] and Gowri Srinivasan[4]
[1] *Computational Earth Science Group (EES-16), Earth and Environmental Sciences Division, Los Alamos National Laboratory, Los Alamos, New Mexico 87545, USA*
[2] *Center for Nonlinear Studies, Theoretical Division, Los Alamos National Laboratory, Los Alamos, New Mexico 87545, USA*
[3] *Department of Civil & Environmental Engineering & Earth Sciences, University of Notre Dame, Indiana 46556, USA*
[4] *Verification and Analysis (XCP-8), X-Computational Physics Division, Los Alamos National Laboratory, Los Alamos, New Mexico 87545, USA*

(Received 3 October 2018; published 25 January 2019)

We characterize the influence of different intersection mixing rules for particle tracking simulations on transport properties through three-dimensional discrete fracture networks. It is too computationally burdensome to explicitly resolve all fluid dynamics within a large three-dimensional fracture network. In discrete fracture network (DFN) models, mass transport at fracture intersections is modeled as a subgrid scale process based on a local Péclet number. The two most common mass transfer mixing rules are (1) complete mixing, where diffusion dominates mass transfer, and (2) streamline routing, where mass follows pathlines through an intersection. Although it is accepted that mixing rules impact local mass transfer through single intersections, the effect of the mixing rule on transport at the fracture network scale is still unresolved. Through the use of explicit particle tracking simulations, we study transport through a quasi-two-dimensional lattice network and a three-dimensional network whose fracture radii follow a truncated power-law distribution. We find that the impact of the mixing rule is a function of the initial particle injection condition, the heterogeneity of the velocity field, and the geometry of the network. Furthermore, our particle tracking simulations show that the mixing rule can particularly impact concentrations on secondary flow pathways. We relate these local differences in concentration to reactive transport and show that streamline routing increases the average mixing rate in DFN simulations.

DOI: 10.1103/PhysRevE.99.013110

I. INTRODUCTION

The behavior of fluid flow and the associated transport of dissolved chemicals through low-permeability subsurface rocks is primarily controlled by fracture networks within the medium. Length scales within these networks typically range several orders of magnitude [1] and characterizing the interplay across these length scales has applications in a range of engineering endeavors including CO_2 sequestration technologies [2], geothermal energy extraction [3], unconventional hydrocarbon extraction [4], and the long-term storage of spent nuclear fuel [5]. At the network structure scale, connectivity and density control the general behavior of the fluid flow field [6]. Within individual fractures, the location of inflow and outflow boundaries and local variations in the fracture aperture determine the local flow field [7,8]. However, how fluid moves through the intersections between fractures is also important in terms of local dispersion because intersections are regions of enhanced mixing [9] and can impact network scale spreading of solute [10].

Discrete fracture networks (DFNs) are one of the most common modeling tools for simulating flow and transport through fractured media. In the DFN methodology fractures are represented as lower dimensional structures in the domain, lines in two dimensions (2D) and planes in three dimensions (3D). The choice to explicitly resolve fractures, as opposed to using effective properties in continuum models, allows observations of transport to be linked to the structural properties of the fracture networks. This choice drastically increases the cost of running DFN simulations and certain aspects of the simulation are modeled as subgrid scale processes.

One such subgrid process is particle behavior within fracture intersections. There have been a number of laboratory experiments [9,11–14] and numerical simulations [15–18] to better understand particle behavior within fracture intersections. The fluid velocity field along fracture intersections is three dimensional and particle behavior is determined by the combination of the velocity field, the velocity magnitude, and diffusion. In a DFN, however, the line of intersection is either a point (2D) or a line (3D) and the true structure of the velocity field is not resolved. In attempts to represent the particle behavior several subgrid processes have been proposed. The two most prominent fracture intersection rules are complete mixing and streamline routing. Particle transport is primarily diffusion controlled with the complete mixing rule and advection dominated with the streamline routing rule. The choice of which process is most appropriate is determined by the local physics of the fracture intersection, characterized by a Péclet number Pe, the ratio of advective to diffusive forces.

---

[*] Corresponding author: jhyman@lanl.gov

2470-0045/2019/99(1)/013110(15)

Assuming complete mixing can be traced to the fracture junction experiments of Krizek *et al.* [11], where an inflowing branch intersected with multiple outflowing branches. In these experiments, tracer from the inflow branch entered a junction and was distributed to the multiple outflowing branches, which was interpreted as complete mixing of the tracer within the junction. In a DFN model with a complete mixing subgrid process, particles enter an intersection and are conceptually allowed to jump between streamlines and mix within the intersection due to diffusion. In contrast, the streamline routing mixing rule prohibits solute from crossing streamlines, implying only advection governs transport, representative of a high Pe condition. Laboratory experimental observations of solute trajectories through a single orthogonal intersection with two inflow and two outflow branches [12–14] suggest streamline routing is appropriate when the intersection $\mathrm{Pe} > O(10)$.

The aforementioned laboratory studies considered transport through an idealized intersection that is poorly representative of real geologic geometries. Moreover, they do not consider the impact of particle behavior along intersections on transport at the fracture and network scale. There have been several numerical simulations to address these aspects of DFN modeling but their conclusions appear to be in disagreement. Park *et al.* [19] concluded that the mixing rule did not significantly impact transport for simulations through two-dimensional networks where fracture lengths were power-law distributed and solute enters the domain via a point-source initial condition. Similarly, Cvetkovic *et al.* [5] simulated transport through a three-dimensional DFN where particles were injected across an inlet plane, and concluded that the mixing rule had little impact on transport as quantified by travel time distributions. However, Kupper *et al.* [20], Park *et al.* [21], and Kang *et al.* [10] found that for a point-source initial condition complete mixing can enhance transverse spreading of a solute plume compared to streamline routing for transport through certain two-dimensional lattice cases. These studies suggest the impact of the mixing rule depends on the network structure, heterogeneity of the velocity field, dimensionality of the network, and initial injection mode of particles. Thus, it is not clear under what conditions the choice of mixing rule at fracture intersections has an impact on different large-scale transport features.

We use DFNWORKS [22] to simulate transport through two different DFN structures that represent varying degrees of structural and velocity field heterogeneity and study conditions under which the mixing rule is important for transport through large-scale fracture networks. One network is a quasi-two-dimensional lattice where the apertures are sampled from a lognormal distribution and the other is a set of networks composed of circular fractures whose lengths are drawn from a power-law distribution. In both sets of simulations, we consider point injection and flux-weighted injection of particles across the entire inlet plane. The impact of complete mixing and streamline routing is compared in terms of the travel time distributions, mean-squared displacement, and transverse breakthrough distributions of solute plumes at uniformly spaced control planes. Additionally, to explore possible implications on mixing driven reactions we also compare mixing rates in simulations with different implemented fracture intersection mixing rules.

We observe that the impact of the mixing rule depends on the initial injection mode, the fracture network structure, and heterogeneity of the velocity field. The greatest impact on upscaled properties is observed when particles are released from a point source. As heterogeneity of the network structure increases particles tend to channelize at the network scale and the impact of the mixing rule on upscaled behavior decreases. But even in highly heterogenous systems, there are significant differences in transport behavior within fracture planes where in-plane channelization is observed. Specifically, we find that streamline routing increases channelization of mass to secondary fractures, resulting in an increased overall system wide averaged mixing rate and local mixing rates that can differ by up to two orders of magnitude. This has strong potential implications for reactive transport, mainly in determining how aggressively and where mixing driven reactions will occur [23,24].

II. DISCRETE FRACTURE NETWORK SIMULATIONS

There are a number of methods used to model flow and the associated transport of dissolved chemical species through fractured media in the subsurface including stochastic continuum [25], dual-porosity/dual-permeability [26], and DFN models [27–29]. Here we use the DFN modeling methodology where individual fractures are represented as planar $(N-1)$-dimensional objects embedded within an N-dimensional space. Each fracture is assigned a shape, location, and orientation within the domain by sampling distributions whose parameters reflect a site characterization. The fractures form a network embedded within an impermeable rock matrix; we do not consider interaction between flow within the fractures and the solid matrix. Each fracture is meshed for computation and the governing equations for flow and transport are numerically integrated on the network. The choice to use a DFN model rather than a continuum model arises due to the focus of this study, which is characterizing the influence of smaller scale processes, namely, particle behavior at fracture intersections, on upscaled transport behavior. Continuum models do not explicitly represent fractures and their intersections and are therefore unsuitable for the task at hand.

The generation of each discrete fracture network along with flow and transport simulations is preformed using the DFNWORKS suite [22]. DFNWORKS is a high-fidelity DFN modeling suite that has been used in analysis of flow properties in fractured media with scales ranging from millimeters to kilometers and with applications in nuclear waste disposal [30,31] and hydraulic fracturing [4,32]. DFNWORKS combines the feature rejection algorithm (FRAM) [33], the LaGriT meshing toolbox [34], the parallelized subsurface flow and reactive transport code PFLOTRAN [26], and an extension of the WALKABOUT particle tracking method [35,36]. FRAM is used to generate three-dimensional fracture networks. LaGriT is used to create a computational mesh representation of the DFN in parallel. PFLOTRAN is used to numerically integrate the governing flow equations. WALKABOUT is used to determine pathlines through the DFN and simulate solute transport. Details of the suite, implementation, its abilities, applications, and references are provided in Hyman *et al.* [22].

A. Flow simulations

Under the assumption of aperture uniformity within a single fracture, flow therein is equivalent to flow between two parallel plates and can be modeled with the Stokes equations, the governing equations for low Reynolds number isothermal single-phase Newtonian flow. The Stokes equations can be integrated to determine the volumetric flow rate Q per unit fracture width normal to the direction of flow

$$\mathbf{Q} = \frac{-b^3}{12\mu}\nabla P, \tag{1}$$

i.e., the Boussinesq equation. Here b is the aperture height and P is pressure. We consider an incompressible fluid such that

$$\nabla \cdot \mathbf{Q} = 0. \tag{2}$$

Equations (1) and (2), along with boundary and initial conditions, are used to derive an elliptic partial differential equation for the steady-state distribution of pressure within a network

$$\nabla \cdot (b^3 \nabla P) = 0. \tag{3}$$

Once the distribution of pressure and volumetric flow rates are determined by numerically integrating (3), the Eulerian velocity field $\mathbf{u}(\mathbf{x})$ within the DFN is reconstructed from the volumetric fluxes and pressures following Makedonska *et al.* [35] and Painter *et al.* [36]. A pressure gradient is imposed, which is aligned with the x axis, making this also the primary direction of flow.

B. Transport simulations: Particle tracking

We represent the transport of a nonreactive conservative solute in the DFN using passive tracer particles, i.e., a Lagrangian approach. Particle motion is purely advective within a fracture and molecular diffusion is only considered in fracture intersections via a subgrid process. We denote the plume of particles as Ω and consider two different inlet conditions. The first inlet condition is a point source where all particles are released into a single fracture close to the center of the inlet plane. In the second inlet condition, particles are spread across the entire inlet plane and the number of particles at a given location is proportional to the flux entering the system at the location, i.e., a flux-weighted injection [30,37,38].

Each particle has a unique initial position that we denote $\mathbf{a} = (0, y, z)^\top$, where the superscript $\top$ indicates the transpose. The trajectory $\mathbf{x}(t; \mathbf{a})$ of a particle starting at $\mathbf{a}$ at time $t = 0$ is given by the advection equation

$$\frac{d\mathbf{x}(t;\mathbf{a})}{dt} = \mathbf{v}_t(t;\mathbf{a}), \quad \mathbf{x}(0;\mathbf{a}) = \mathbf{a}, \tag{4}$$

where the Langrangian velocity $\mathbf{v}_t(t;\mathbf{a})$ is given in terms of the Eulerian velocity $\mathbf{u}(\mathbf{x})$ as

$$\mathbf{v}_t(t;\mathbf{a}) = \mathbf{u}[\mathbf{x}(t;\mathbf{a})]. \tag{5}$$

The length $\ell(t;\mathbf{a})$ of the trajectory at a time t is

$$\frac{d\ell(t;\mathbf{a})}{dt} = v_t(t,\mathbf{a}), \tag{6}$$

where the Lagrangian velocity is the velocity magnitude $v_t(t,\mathbf{a}) = |\mathbf{v}_t(t,\mathbf{a})|$. The length of the pathline, ℓ, is used to parametrize the spatial and temporal coordinates of the particle.

Within the domain, we consider uniformly spaced control planes that are perpendicular to the primary direction of flow. The first arrival time $\tau(x_i;\mathbf{a})$ of a particle at a control plane located at x_i from the inlet is given by

$$\tau(x_i;\mathbf{a}) = t[\lambda(x_i);\mathbf{a}], \quad \lambda(x_i) = \inf\{\ell | x_i(\ell;\mathbf{a}) \geqslant x_i\}. \tag{7}$$

C. Measurements

At every control plane x_i, the first arrival times of the particles [Eq. (7)] are combined to obtain the cumulative distribution of travel times for the plume of particles:

$$\psi(t, x_i) = \frac{1}{M}\int d\Omega\, H[t - \tau(x_i, \mathbf{a})]. \tag{8}$$

Here, M is the total mass of all the particles $M = \int d\Omega$ and $H(t)$ is the Heaviside function. We refer to $\psi(t, x)$ as the breakthrough curve. We also compute the transverse spreading using the distribution of particle positions at each control plane. Denoting the position of each particle at the control plane x_i as $\mathbf{z}_x$ the transverse breakthrough position distribution (TBPD) in z is

$$f_{x_i}(z_k) = \frac{1}{M}\int d\Omega\, \delta(z_k - \mathbf{z}_{x_i}), \tag{9}$$

where δ is the Dirac delta function. An analogous equation is used to calculate TBPD in y.

The characteristic spreading of the particle plume in the transverse direction at longitudinal position x is quantified by the mean-squared displacement,

$$\mathrm{MSD}_x = \frac{1}{M}\int d\Omega (\bar{\mathbf{z}}_x - \mathbf{z}_x)^2 + (\bar{\mathbf{y}}_x - \mathbf{y}_x)^2, \tag{10}$$

where $\mathbf{z_x}, \mathbf{y_x}$ are vectors of the transverse position for each particle at x and the overline denotes the average over all particles.

III. PARTICLE BEHAVIOR AT FRACTURE INTERSECTIONS

When a particle arrives at a fracture intersection, both advective and diffusive processes should govern motion through the intersection. In a purely advective system, particle motion follows the streamlines of the velocity field. However, diffusion enables particles to jump between streamlines and mix. The amount of mixing that occurs in a fracture intersection is a balance of the strength of advection relative to diffusion which can be characterized by Péclet number

$$\mathrm{Pe} = \frac{vL}{2D_m}. \tag{11}$$

We adopt the Pe definition provided in [15] where v is the average velocity within the intersection, L is a characteristic diagonal distance across the intersection, and D_m is the molecular diffusion coefficient.

The upscaled nature of DFN models prevents the detailed physics that control mass transfer at fracture intersections from being resolved. Instead, subgrid processes are used to

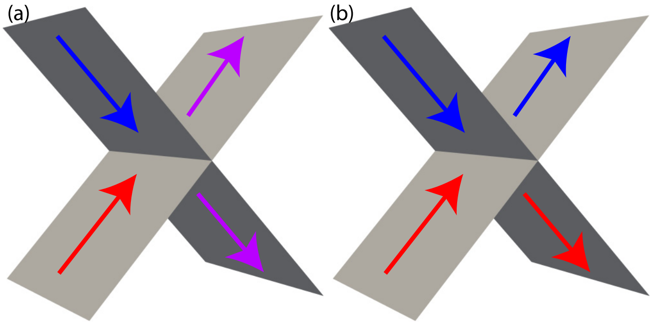

FIG. 1. A fracture intersection with two inflow branches and two outflow branches. All branches have equivalent discharge magnitudes. In complete mixing (a) mass from both inlets (red and blue) mix at the intersection and mass is distributed equally to each outlet (purple). In streamline routing (b) incoming red mass from the bottom inlet and blue mass from the top inlet are forced to their respective adjacent fractures and do not mix.

model mass transfer through intersections. There are two mixing rules that are commonly applied: (1) complete mixing and (2) streamline routing. These rules are representative of end members associated with diffusion and advective controlled transport, respectively. The choice of which rule to apply should reflect the physics of the intersection, as determined by the Pe.

At a fracture intersection, conservation of mass requires that the sum of incoming and outgoing Darcy fluxes is zero, $\sum_i q_i = 0$. Both mixing rules require knowledge of the Darcy outflowing fluxes. The streamline routing rule needs additional information, the position of the inflow branches relative to each outflow branch, and so implementation of complete mixing at fraction intersections is simpler than streamline routing.

A. Complete mixing

Under complete mixing, particle motion within the intersection is controlled by diffusion. In this scenario, particles enter an intersection inlet and are conceptually allowed to jump between streamlines by being repositioned to any point within the intersection with equal probability. Figure 1(a) shows mass transfer under the complete mixing rule in a single orthogonal intersection where all branches have an equivalent discharge magnitude. Light-blue mass from the top inlet and red mass from the bottom inlet mix at the intersection and are distributed equally between the two outflowing branches. Each outlet contains mass from both inlets, represented by the outflowing purple color in the figure.

With complete mixing the probability a particle exits a given outlet is proportional to the outlet flux, mathematically represented as

$$p_j = \frac{|q_j|}{\sum_k |q_k|}, \tag{12}$$

where p_j is the probability a particle exits outlet j, and k denotes an outflowing fracture branch.

B. Streamline routing

In the streamline routing rule particle motion through fracture intersections is advection controlled. Particles adhere to their respective streamlines through the intersection, as if no mixing occurs within the intersection. Therefore, particle motion depends on the particle's inlet position. The streamline routing rule differs from the complete mixing rule only when a fracture intersection has multiple incoming and multiple outflowing branches. In a two-fracture intersection there are only two intersection types that have this geometry: (a) continuous junctions and (b) discontinuous junctions [13].

A continuous junction has two inflowing branches, two outflowing branches, and the inflowing branches are adjacent, i.e., lie on different fractures. Figure 1(b) depicts streamline routing mass transfer through a continuous junction where all branches have equivalent discharge magnitudes. Flow from an inlet is directed to the outflowing adjacent branch. In this case, all mass from each inlet is distributed to the adjacent outflowing branch because there is no mixing within the fracture intersection. In general, the streamline routing rule goes as follows. If discharge from the inlet is less than the adjacent outlet discharge, all mass is directed to the adjacent outlet. If the inlet discharge exceeds the adjacent outlet discharge, conservation of mass requires that the adjacent outlet is filled and excess mass is directed to the other outlet.

Consider a particle entering a continuous junction from an inlet with flux q_{in}, which is adjacent to an outflow branch with flux q_{adj}. The second (opposite) outflow branch lies on the same fracture as the initial inlet fracture and has flux q_{opp}. The streamline routing rule dictates that the probabilities of transitioning from the inlet to the adjacent p_{adj} and opposite p_{opp} outflow branches are

$$p_{\mathrm{adj}} = \begin{cases} 1, & q_{\mathrm{adj}} \geqslant q_{\mathrm{in}} \\ \frac{q_{\mathrm{adj}}}{q_{\mathrm{in}}}, & q_{\mathrm{adj}} < q_{\mathrm{in}} \end{cases}, \quad p_{\mathrm{opp}} = 1 - p_{\mathrm{adj}}. \tag{13}$$

More details on continuous junctions are found in Hull and Koslow [13].

Discontinuous junctions arise from multiple sources and sinks present in the fracture network, such as a geothermal field with production and injection wells [13]. In a discontinuous junction inflowing branches are opposite and lay on the same fracture. Hull and Koslow [13] proposed two distributions of streamline routing through a four-branch discontinuous intersection, one equivalent to complete mixing and one where the high discharge inlet is preferentially directed to the high discharge outlet. Philip [39] extended Hull's analysis by finding solutions for Laplace and Stokes flow through the orthogonal intersections. Philip showed that under certain conditions, mainly when there are significant differences in branch discharge magnitudes, using complete mixing for streamline routing can result in significant error. However, Hull's other proposed streamline routing rule, where the high discharge inlet is preferentially directed to the high discharge outlet, is also prone to error as adjacent streamlines can have opposite directions for a considerable distance. Hence, the theory for streamline routing through discontinuous intersections is still not fully developed. For completeness, we present Hull's second proposed streamline routing rule for discontinuous intersections. In this case, mass from the higher discharge incoming branch $q_{\text{in}}^{\text{max}}$ is partitioned to the higher discharge outflowing branch $q_{\text{out}}^{\text{max}}$ and any excess mass exits the smaller discharge outflowing branch $q_{\text{out}}^{\text{min}}$. A particle arriving from the inlet with $q_{\text{in}}^{\text{max}}$ has outlet transition probabilities given by

$$p_{\text{out}}^{\text{max}} = \begin{cases} 1, & q_{\text{out}}^{\text{max}} \geqslant q_{\text{in}}^{\text{max}} \\ \frac{q_{\text{out}}^{\text{max}}}{q_{\text{in}}^{\text{max}}}, & q_{\text{out}}^{\text{max}} < q_{\text{in}}^{\text{max}} \end{cases}, \quad p_{\text{out}}^{\text{min}} = 1 - p_{\text{out}}^{\text{max}}. \tag{14}$$

A particle arriving from the weaker inflow branch has transition probabilities:

$$p_{\text{out}}^{\text{max}} = \begin{cases} \frac{q_{\text{out}}^{\text{max}} - q_{\text{in}}^{\text{max}}}{q_{\text{in}}^{\text{min}}}, & q_{\text{out}}^{\text{max}} \geqslant q_{\text{in}}^{\text{max}} \\ 0, & q_{\text{out}}^{\text{max}} < q_{\text{in}}^{\text{max}} \end{cases}, \quad p_{\text{out}}^{\text{min}} = 1 - p_{\text{out}}^{\text{max}}. \tag{15}$$

We performed simulations using both of Hull's discontinuous streamline routing rules. Results were not affected by different rules due in part to the observation that discontinuous intersections are rare in the systems under consideration. Our presented results are only shown for the case described above.

The occurrence and frequency of triple intersections, where three fractures come together at a point, depends on the particular fractured media under consideration. However, these triple intersections do occur regularly in unconstrained stochastically generated DFNs, and their frequency depends on the fracture length distribution, network density, and fracture family orientation. Thus, from a practical and computational point of view, a rule for particle behavior at these points needs to be adopted in DFN modeling. We apply complete mixing at all triple intersections primarily due to the lack of experimental data concerning flow properties at triple intersections by which to verify appropriate streamline routing rules.

IV. RESULTS

A. Sample fracture networks

We consider flow and transport within two distinct fracture network structures. The first is a quasi-two-dimensional lattice network and the second is a set of stochastically generated networks, where fracture radii are sampled from a truncated power-law distribution. These two network structures are considered because they display different features that drive flow channelization. The lattice networks have an idealized, regular geometry and flow channelization arises from variations in the permeability field. In the truncated power-law networks, fracture intersections are less frequent and the geometry of the network drives flow channelization. In the analysis of results we nondimensionalize distance with l^*, the maximum fracture radius in the system, and time with τ^*, the time required to traverse l^* traveling at the mean particle velocity.

1. Lattice network

The lattice network is comprised of two sets of 50 parallel three-dimensional planar fractures, where fractures in each set are spaced one meter apart and intersect fractures of the other sets at a 45° angle. The computational domain has sizequery, [32, 1, 16] m in the x, y, z directions. A pressure gradient of 1 MPa is used to drive flow in the x direction. The imposed pressure field results in a quasi-two-dimensional velocity field because velocity in y is negligible.

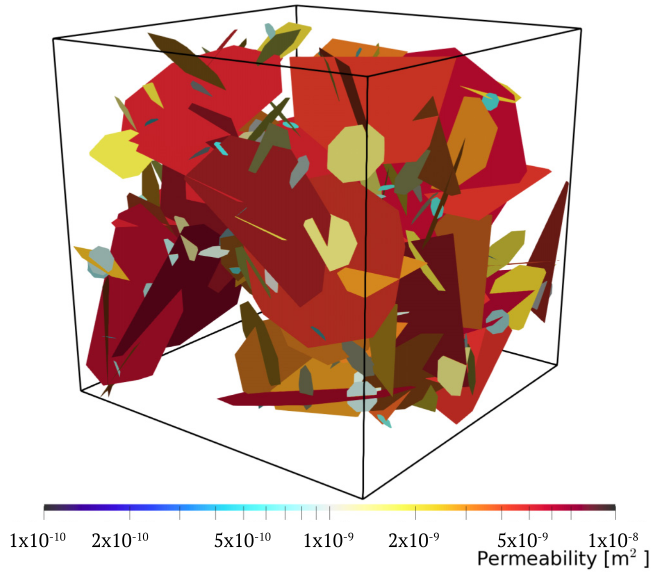

FIG. 2. One realization of a DFN with fracture lengths drawn from a power-law distribution. Fractures are colored by their permeability, which is positively correlated with fracture radius.

Fracture apertures are sampled from a lognormal distribution in accordance with observations [40–42]. Each lattice network has a mean aperture $\overline{b} = 10^{-4}$ m and three aperture variance cases are considered, $\sigma^2_{\ln(b)} = 0.1, 0.5, 1$. Twenty-five realizations are generated for each mixing rule and aperture variance combination. For each combination, transport is simulated for both point source and flux-weighted initial injections. These simulations are similar to the 2D lattice simulations of Kang *et al.* [10]. However, in our experiments velocity field heterogeneity is controlled by changing the distribution of aperture sizes and we consider an additional flux-weighted initial injection case. The objective of studying this network set is to fix the network structure and focus on the effects of variability at the fracture scale.

2. Truncated power-law network

The second set of networks is composed of disk-shaped fractures whose radii are sampled from a truncated power-law distribution (Fig. 2), which is a commonly observed length distribution in field data [1,43–45]. Bour and Davy [43] showed a power-law distribution accurately captures the wide range of fracture lengths often observed in geological datasets [44,45]. In our power-law networks, fracture radii are sampled from a truncated power-law distribution with exponent α and upper and lower cutoffs of $(R_u; R_0)$:

$$R = R_0 \left[1 - \eta + \eta \left(\frac{R_0}{R_u} \right)^{\alpha} \right]^{-1/\alpha}, \tag{16}$$

where η is a random number sampled from a uniform distribution on [0,1]. We choose an exponent $\alpha = 2.1$ and cutoffs $R_0 = 2R_u = 30$ m based on field data [1,46]. The networks are not meant to be realizations of the networks reported in [1]

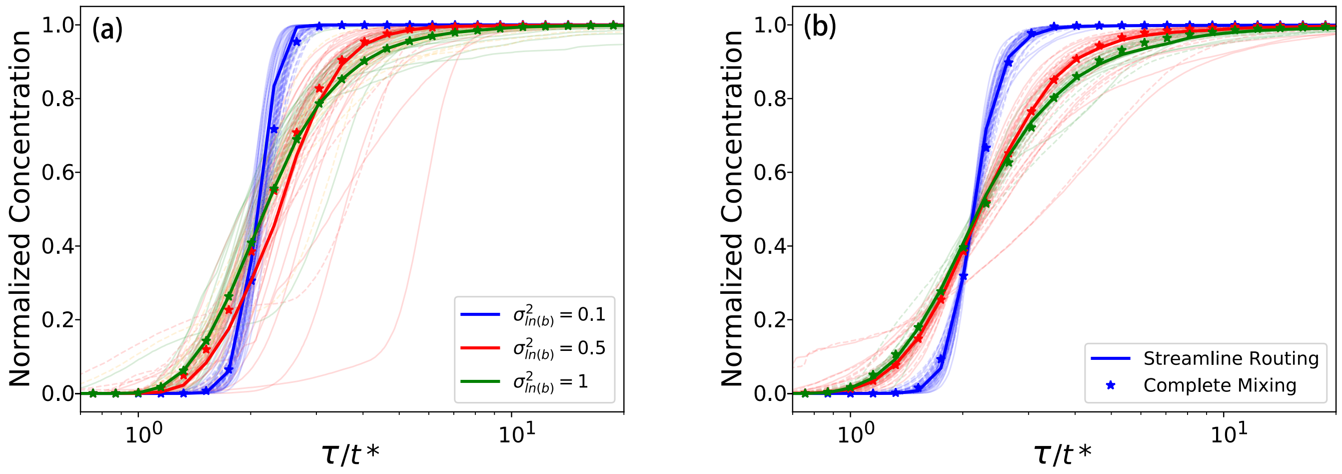

FIG. 3. Cumulative distribution of first passage arrival times (breakthrough curves) for point injection (a) and flux-weighted (b) initial condition. Thick lines are median breakthrough curves for 25 realizations and transparent lines correspond to single realizations. For each realization, solid lines indicate streamline routing and dashed lines indicate complete mixing. Colors correspond to different aperture variances; $\sigma^2_{\ln(b)} = 0.1, 0.5, 1$ are depicted with blue (steepest slope), red, and green (least steep slope), respectively.

and [46], but rather semigeneric fracture networks. Fracture orientations are uniformly random and centers are uniformly distributed throughout the domain. Fracture apertures are positively correlated to their radius, $b = 5 \times 10^{-5}\sqrt{R}$, which controls the hydraulic properties within the fracture. This correlation between fracture size and aperture is common in DFN models [29,31,47–50]. The computational domain is a cube with sides of length 100 m. We refer to these as truncated power-law (TPL) networks.

Ten independent identically distributed network realizations are generated. We stop the generation of the networks once 1000 fractures are accepted into the network. This results in a network that is about seven times denser a network at the percolation threshold defined by [7,51]. This procedure ensures that there is a subnetwork that connects inflow to outflow boundaries. To reduce computational cost, we remove all isolated clusters of fractures, those that that do not connect inflow to outflow boundaries, because they do not contribute to flow. There are roughly 200 fractures in the final networks and the average fracture intensity (P_{32}: surface area over total volume) is approximately 0.1. Flow is forced along the x axis by imposing constant pressure conditions at the inlet and outlet control planes perpendicular to x. The pressure difference in x across the inflow and outflow boundary is 1 MPa.

B. Lattice network simulations

1. *Breakthrough curves: Lattice*

Figure 3 shows the cumulative distribution of first passage arrival times [Eq. (8)] for the point injection (a) and flux-weighted (b) initial conditions. Thick lines (streamline routing) and stars (complete mixing) are median breakthrough curves for 25 realizations and transparent lines correspond to single realizations. For each realization, solid lines indicate streamline routing and dashed lines indicate complete mixing. Colors correspond to different aperture variances; $\sigma^2_{\ln(b)} = 0.1, 0.5, 1$ are depicted with blue, red, and green, respectively. As velocity field heterogeneity decreases, breakthrough curve realizations homogenize and the range of arrival times decreases. In both injection conditions and for all values of $\sigma^2_{\ln(b)}$ there is little impact of the mixing rule on the median observed travel time distributions. In turn, these results indicate that the mixing rule has no major impact on mean particle velocities, demonstrated by no significant change in breakthrough curve behavior (Fig. 3). Additionally, breakthrough curve realizations are more clustered near the median breakthrough curve for the flux-weighted initial condition, e.g., the range of P_{50} values, the time at which 50% of mass has crossed the outlet control plane, decreases with the flux-weighted case.

2. *Solute spreading: Lattice*

Figure 4 shows the spatial evolution of the transverse breakthrough position distribution $f_{x_i}(z)$ for simulated flow and transport through single realizations of lattice networks of varying velocity field heterogeneities with a point source injection initial condition. The top row shows $f_{x_i}(z)$ for complete mixing, the middle is for streamline routing, and the bottom shows the ratio of streamline routing to complete mixing transverse breakthrough position concentrations. In each column, the streamline routing and complete mixing lattice networks are identical realizations. Colors are the logarithm of the concentration with yellow corresponding to relatively high concentration values and blue corresponding to lower values. In both mixing rule cases, there is more pronounced flow channeling as $\sigma^2_{\ln(b)}$ increases due to the formation of paths of lower resistance. We calculate the percent of particles concentrated on each fracture at each control plane. As heterogeneity increases from $\sigma^2_{\ln(b)} = 0.1$ to $\sigma^2_{\ln(b)} = 1$, the largest value of percent particles on a single fracture increases by nearly a factor of 2 at distances greater than $x/l* > 1$, demonstrating increased flow channelization (results not shown).

When complete mixing is used, the particles disperse transversely faster than in this case of streamline routing and the plume reaches the lateral boundary of the domain

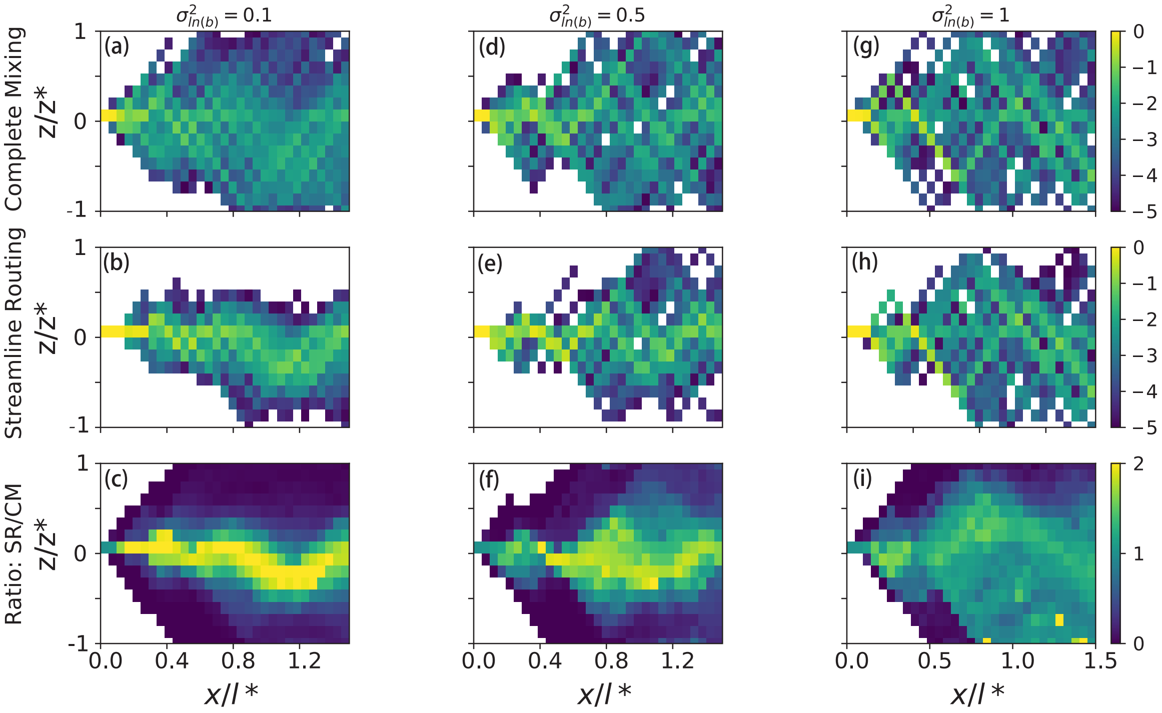

FIG. 4. The transverse distribution at sequential control planes through a lattice network with a point injection initial condition for one realization. All lattices have the same mean aperture size. Variance of aperture size is selected from a lognormal distribution and increases from the left to right column. Simulations are completed for complete mixing (row 1) and streamline routing (row 2) intersection rules for the same network realization. Row 3 gives the ratio of streamline routing to complete mixing transverse breakthrough position concentrations. Colorbars show log probabilities (rows 1 and 2) and absolute ratio values (row 3). Complete mixing enhances particle spreading. As velocity field heterogeneity increases, the impact of the mixing rule on particle spreading decreases. The transverse direction z is normalized by half the length the of domain z^*.

closer to the inlet. By contrast, streamline routing increases channelization, which is most notable at low values of $\sigma^2_{\ln(b)}$. Hence, both streamline routing and increasing velocity field heterogeneity increase channelization of particles. The ratio of the streamline to complete mixing TBPD highlights how the evolution of $f_{x_i}(z)$ changes because of the intersection mixing rule. Areas of dark blue have value 0, indicating positions where breakthrough occurred under complete mixing but not streamline routing. The yellow areas through the center of the lattice show fractures where streamline routing increases particle concentration.

Figure 5 shows the same plots as in Fig. 4 for a flux-weighted injection. Only the $\sigma^2_b = 0.5$ is provided as all σ^2_b values displayed nearly identical behavior. The ratio of streamline routing to complete mixing for $f_{x_i}(z)$ is close to 1 throughout much of the domain, indicating nearly identical

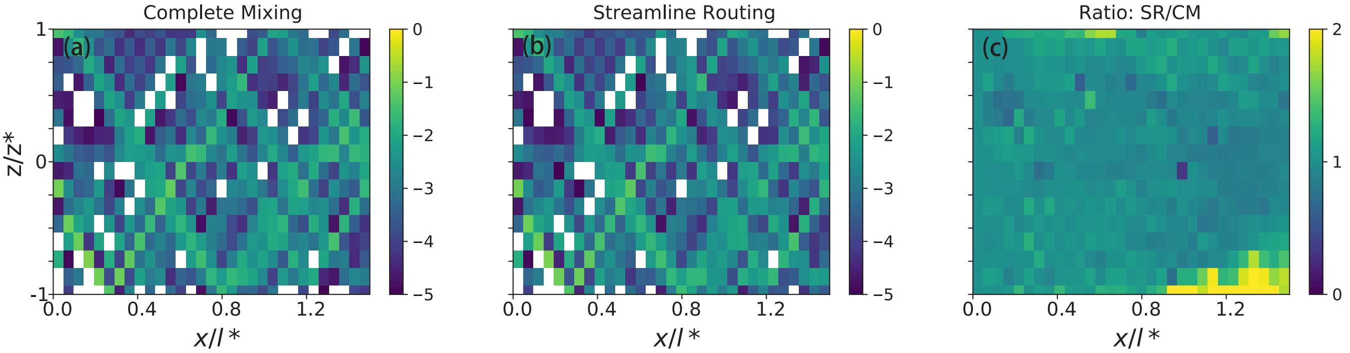

FIG. 5. The transverse breakthrough position distribution at each control plane for one realization of the lattice with a flux-weighted injection. Simulations are completed for complete mixing (a) and streamline routing (b) intersection rules. (c) gives the ratio of streamline routing to complete mixing transverse breakthrough position concentrations. Colorbars show log probabilities [(a) and (b)] and the absolute ratio (c). $\sigma^2_{\ln(b)} = 0.5$ is the only aperture variance shown because results do not significantly change for different velocity field heterogeneities. The mixing rule has less impact on particle spreading with a flux-weighted initial condition. The transverse direction z is normalized by half the length of domain z^*.

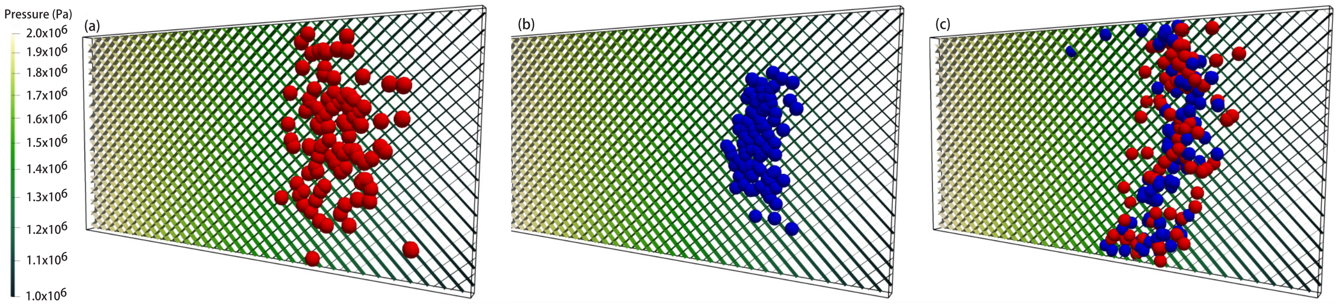

FIG. 6. Particles within the quasi-two-dimensional lattice network. In (a) and (b), particles injected from the same point source on the left boundary and driven right by a pressure gradient. In (a), particles adhere to a complete mixing rule (red) and in (b) they follow streamline routing (blue). The choice of a complete mixing rule in combination with a point injection leads to higher transverse dispersion than if streamline routing is used under the same initial conditions. (c) shows particles injected using flux weighting adhering to both mixing rules (red: complete mixing/blue: streamline routing). Here, no significant difference between the distribution of particle locations between the two rules is observed.

distribution of the solute plume for the two mixing rules. One exception is the area of yellow in the bottom-right corner of the ratio figure (c), where streamline routing has a higher particle concentration. This is an area of low particle concentrations and is therefore more sensitive. The results presented here indicate that the mixing rule's impact on the evolution of $f_{x_i}(z)$ is less significant when particles are injected using a flux-weighted initial condition.

To demonstrate these differences, Fig. 6 shows particles within one realization of the lattice network with $\sigma^2_{\ln(b)} = 1.0$ where fractures are colored by pressure. (a) is a snapshot of particles injected from a point injection where the complete mixing rule is applied and in (b) streamline routing is applied. As discussed above, the application of the complete mixing rule leads to higher transverse dispersion when compared to streamline routing. (c) shows both particles (red: complete mixing/blue: streamline routing) injected using flux weighting. Here, no significant difference between the distribution of particle locations between the two rules is observed.

Figure 7 shows the mean value of the MSD for point (a) and flux-weighted (b) initial conditions. These are calculated at each control plane by averaging over all particles and all 25 realizations. Solid lines indicate streamline routing and stars indicate complete mixing. Colors correspond to different aperture variances; $\sigma^2_{\ln(b)} = 0.1, 0.5, 1$ are depicted with blue, red, and green, respectively.

For the point injection, there is a significant difference between the observed MSD values for complete mixing and streamline routing. For all values of $\sigma^2_{\ln(b)}$ complete mixing results in an increased MSD. The impact of the mixing rule on MSD decreases with increasing velocity field heterogeneity, shown by a decreasing difference in MSD between mixing rules. For the flux-weighted injection the mixing rule's impact on MSD is less than in the point injection case, as the complete mixing and streamline routing curves more closely match. Note that the MSD is driven by displacements in the z direction due to the quasi-2D nature of the lattice.

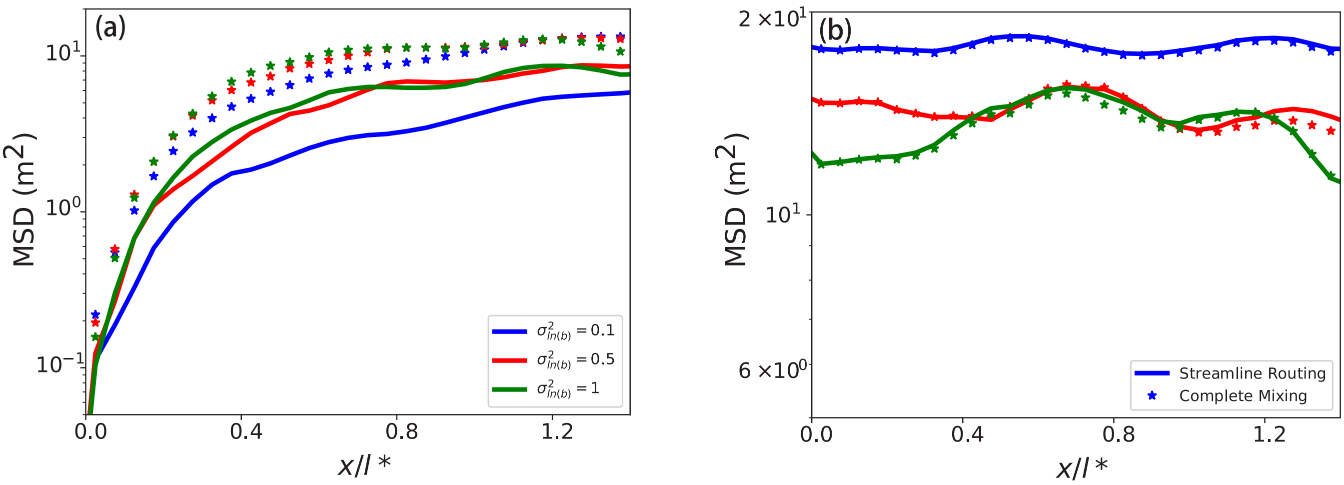

FIG. 7. The mean MSD in the lattice network is calculated at each control plane by averaging over all particles and all 25 realizations. Solid lines indicate streamline routing and stars indicate complete mixing. Plotted is MSD for both the point (a) and flux-weighted (b) initial conditions. Colors correspond to different aperture variances; $\sigma^2_{\ln(b)} = 0.1, 0.5, 1$ are depicted with blue [upper curve in (b)], red, and green [lower curve in (b)], respectively. As velocity field heterogeneity increases the mixing rule's impact on MSD decreases. A flux-weighted injection results in less spatial variability of MSD.

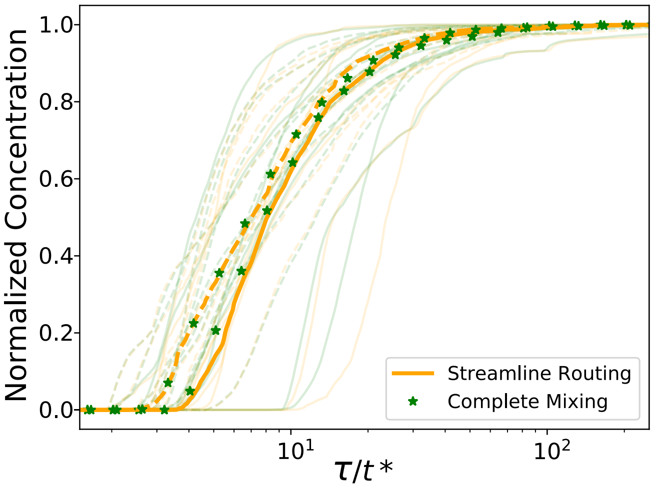

FIG. 8. Median breakthrough curves of ten TPL realizations for complete mixing (green stars) and streamline routing (thick orange lines). Solid lines correspond to point injections and dashed lines correspond to a flux-weighted initial condition. Each breakthrough curve realization is plotted with a transparent line. The mixing rule has a negligible impact of the distribution of arrival times. A flux-weighted initial condition homogenizes the spread of breakthrough curves.

In the point injection, the number of times particles change fractures averaged over all particles and over 25 realizations increases for streamline routing by 52, 36, and 33% for $\sigma^2_{\ln(b)} = 0.1, 0.5, 1$, respectively. As the velocity field heterogeneity increases, particles change fractures less frequently due to increased channelization to high discharge pathways. In the case of flux-weighted injection, streamline routing increases the mean number of times a particle changes fractures by 52, 39, and 36% for $\sigma^2_{\ln(b)} = 0.1, 0.5, 1$ compared with complete mixing. Again as the velocity field heterogeneity increases particles change fractures less often and more particles are channelized to high discharge fractures.

C. Power-law networks simulations

1. Breakthrough curves: TPL network

The median breakthrough curves through the ten TPL realizations for complete mixing (green stars) and streamline routing (thick orange lines) are shown in Fig. 8. Solid lines correspond to point injections and dashed lines correspond to a flux-weighted initial condition. Each breakthrough curve realization is plotted with a transparent line. No significant difference in the breakthrough curves is observed between the two mixing rules indicating that the choice of mixing rule has a negligible impact of the distribution of arrival times. The breakthrough curve is changed in two ways when using the flux-weighted injection. First, breakthrough curves are shifted left, meaning particles on average traverse the entire network in less time compared with a point injection. This indicates that on average, the selected flow paths resulting from the sampled point injection in this study are slower than the fluxed-weighted velocity average. However, given a larger sample of networks, we expect median breakthrough curves to converge. Second, the variability in breakthrough arrival times decreases with the flux-weighted injection; the flux-weighted breakthrough curves are more clustered near the median, whereas the point injection breakthrough curves display greater variation in arrival time for an associated cumulative concentration value.

2. Solute spreading: TPL network

Figure 9 shows the transverse breakthrough position distributions in z for one realization of a truncated power-law distributed radii network for the point (a) and flux-weighted (b) injection modes. The percent of particles on primary fractures remains similar across mixing rules and over 50% of particles at a given control plane are concentrated on less than 10% of the total fractures in the system. In the case of point injection, there are primary fractures as indicated by the brightly colored areas lying between 0 and 0.5 in $z/z*$. Between 0 and 2 x/l^* there is a relatively low number of fracture intersections and particle trajectories are similar. In this region the ratio of streamline routing to complete mixing TBPD is $O(1)$. At a distance greater than 2 in x, the fracture intersection density increases and complete mixing more evenly distributes particles across secondary fractures, observed as a more uniform color in TBPD distributions. In streamline routing, increased channelization to secondary fractures is observed as an increased number of streaks in the TBPD, particularly prevalent in the top and bottom right corners of the TBPD figures. These streaks also appear as yellow areas in the bottom figure that shows the ratio of the concentration for the two rules.

With a flux-weighted initial condition, the mixing rule again causes significant differences in TPBD on secondary fractures, observed as an increased number of streaks in the streamline routing simulations. However, the general evolution of particle spreading remains similar. Areas of high particle concentration (green and yellow colors) are similar for each mixing rule. There is a primary fracture (brightly colored) that extends from 1 to 2 in x and 0 to 0.5 in z that has a streamline routing TBPD to complete mixing TBPD of $O(1)$, indicating particle concentration on this fracture is approximately equal.

Figure 10 shows the MSD, averaged over all particles in the ten realizations of TPL networks, for complete mixing (green) and streamline routing (orange) with a point (solid lines) and flux-weighted (dashed lines) injection. There is less spatial variability in MSD for the flux-weighted injection condition. As opposed to the lattice, the complicated network structure constrains the spreading of particles thereby limiting the impact of the mixing rule on MSD. The observed channelization due to streamline routing has a small impact on average particle behavior. The mean (averaged over all particles and all realizations) number of times a particle changes fractures from inlet to outlet increases approximately 5% from 7.7 in complete mixing to 8.0 in streamline routing. This change percentage is less than in the lattice because the fracture intersection density is lower in the TPL networks. Consistent with the point injection on the lattice, MSD increases with increasing distance from the initial point of injection.

In the case of the flux-weighted injection, the mean number of times particles change fractures increases 5% from

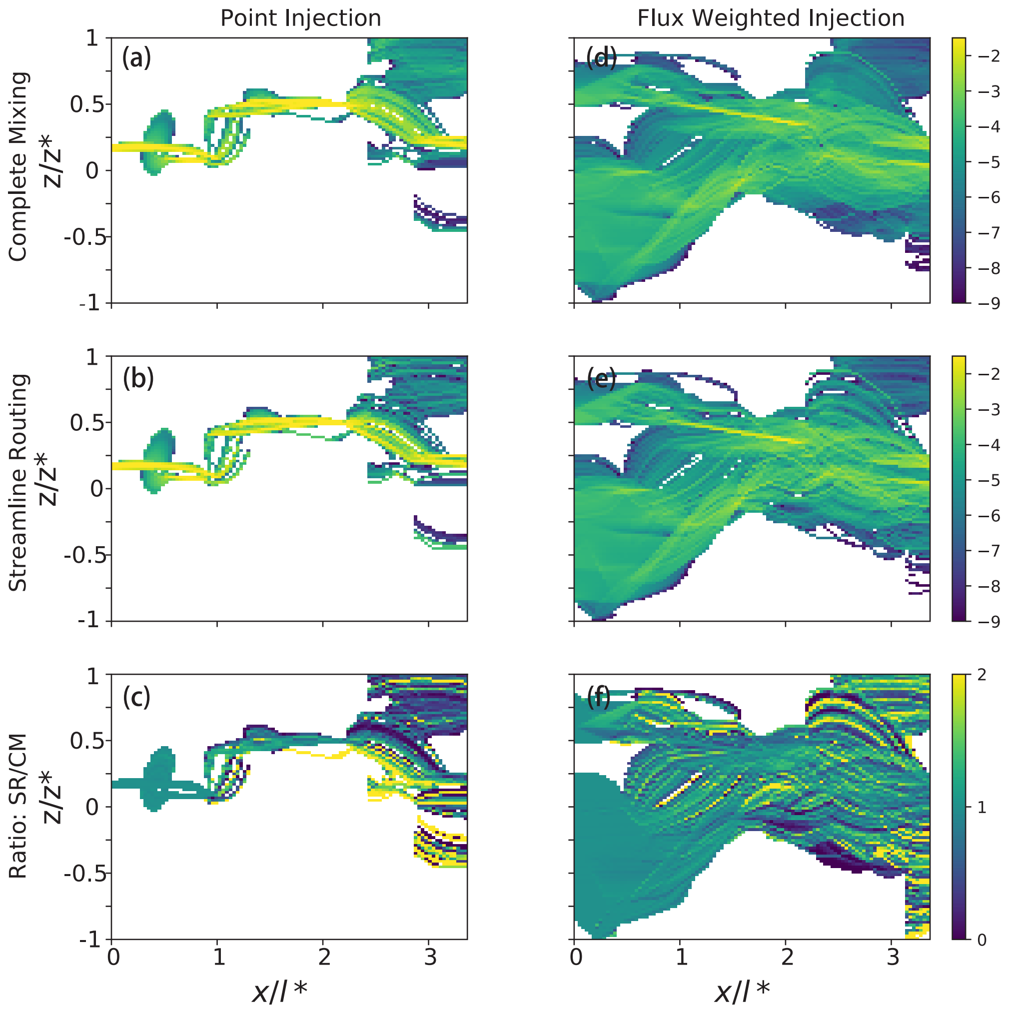

FIG. 9. The transverse breakthrough z-position distribution for one realization of a TPL network for a point (left column) and flux-weighted (right column) initial injection mode. Simulations are completed for complete mixing [row 1: (a) and (d)] and streamline routing [row 2: (b) and (e)] intersection rules. Row 3 gives the ratio of streamline routing to complete mixing transverse breakthrough position concentrations. Colorbars show log probabilities [rows 1 and 2: (a), (b), (d), and (e)] and the absolute ratio value [row 3: (c) and (f)]. Streamline routing increases channelization of particles to secondary fractures, shown as areas of yellow in the ratio figures. The transverse direction z is normalized by half the length of domain z^*.

6.2 for complete mixing to 6.5 for streamline routing. The flux-weighted initial condition increases the initial spread of particles compared to the point injection, which allows transverse breakthrough to occur across a larger portion of the domain. Hence, the flux-weighted injection increases MSD at all measured control planes. As was the case for the point injection, the MSD values are nearly the same for both mixing rules. Similar to the lattice flux-weighted injection simulations, MSD remains relatively constant as distance from the inlet increases, with spatial changes resulting from the network structure and not the mixing rule.

V. DISCUSSION

The results of the simulations presented in the previous section indicate that there are scenarios where the choice of mixing rule at fracture intersections can have a large impact on transport behavior and other scenarios where the impact is negligible. As noted in the introduction, this is consistent with the literature where seemingly opposite statements are made with regard to how important is the mixing rule. The magnitude of the mixing rule's influence is determined by how particles enter the network, the complexity of the fracture network, and the heterogeneity of the velocity field.

A. Injection mode

There are two major differences between the flux-weighted and point injection modes that cause differences in solute spreading. First, a point injection releases particles onto one fracture and all particles are influenced by the same local effects near the injection point. Therefore, the initial behavior is highly dependent on where the particles are released. The flux-weighted initial condition spreads particles across the entire inlet, thereby reducing the impact of such local effects and reflecting a more broad statistical sampling of the heterogeneous system. Second, a flux-weighted injection channelizes particles to high discharge fractures from the

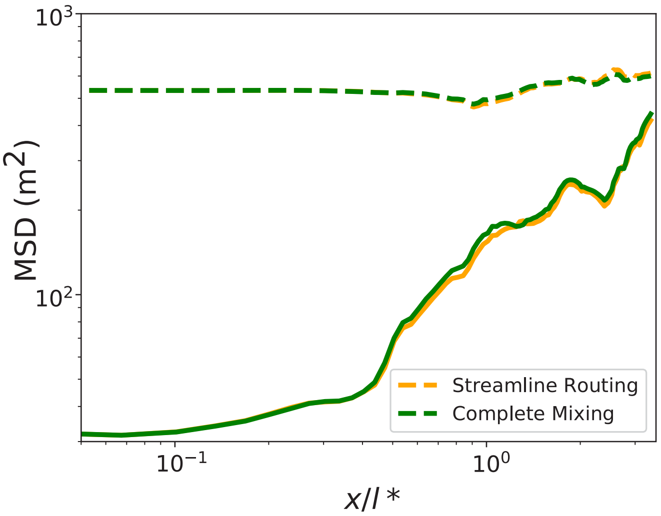

FIG. 10. The MSD is averaged over all particles in ten realizations of stochastically generated TPL networks for complete mixing (green) and streamline routing (orange) with a point (solid lines) and flux-weighted (dashed lines) injection. The MSD for the flux-weighted injections has less spatial variability. The network structure drives particle spreading and so the impact of the mixing rule on MSD is negligible.

start of the simulation. The flux-weighted injection weights high discharge fractures more than low discharge fractures by distributing particles proportionally to fracture discharge, meaning particles channelize on primary fractures immediately. As a fracture's discharge increases the probability of a particle leaving that fracture decreases. Thus the mixing rule's impact decreases as more particles are distributed to high discharge fractures because particles preferentially remain on these high discharge pathways. This decreased impact is demonstrated by similar TPBD evolution for each mixing rule when particles are flux-weight injected.

In a large enough network, the initial distribution of Lagrangian velocities evolves to an asymptotic stationary distribution, where Langrangian velocities become proportional to the local velocity field, i.e., the transverse concentration distribution for the point injection will converge to the flux-weighted injection concentration distribution. The time needed for this to occur can be characterized with a Taylor-like timescale, $T_T = \frac{a^2}{D_T}$, where a is a characteristic length and D_T is effective dispersion. In both network structures we observe that the point-injected MSD approaches the flux-weighted MSD as distance (and time) from particle release increase. Note that a and D_T are strongly affected by the network geometry and so T_T changes with varying network structures. Additionally, the mixing rule influences D_T; mainly complete mixing increases D_T, and thus T_T decreases.

In a regularized geometry, such as the lattice, we observed complete mixing enhances initial particle spreading for a point injection (Fig. 4). At the length scales considered, the point injection breaks Lagrangian ergodicity, that is, the Lagrangian velocity statistics sampled along a particle trajectory is not equivalent to an ensemble average across all particle velocities. Dentz *et al.* [52] showed that in steady heterogeneous flows, a Lagrangian distribution found by spatially sampling along particle trajectories is stationary if the initial particle velocity distribution is equivalent to the Eulerian flux-weighted velocity distribution. Once sufficient time has passed and the initial condition is erased, ergodicity is established and the mixing rule becomes negligible for transverse particle spreading (Fig. 5). Since ergodicity is not established at preasymptotic times for a point injection, the mixing rule does impact spreading on the lattice. However, in networks with highly heterogeneous structures, network geometry becomes increasingly important and the impact of the injection mode decreases. For example, in the TPL networks there is a relatively small number of fracture intersections and so particle transport is constrained by the network geometry and the injection mode and the mixing rule has negligible impact even at preasymptotic times (Fig. 9).

B. Network structure

A fracture network's geometry, specifically the fracture intersection density and fracture orientation, constrains plume spreading. As the fracture intersection density increases, particles have an increased probability of changing fractures. The lattice network has a higher density of fracture intersections than the TPL networks and all intersections are continuous junctions, i.e., incoming inlets are adjacent. Therefore the mixing rule more significantly impacts particle spreading behavior. In continuous junctions, streamline routing increases the probability of changing fractures (to the adjacent) by a factor of $\frac{q_{\text{adj}}+q_{\text{opp}}}{q_{\text{adj}}}$ or $\frac{q_{\text{adj}}+q_{\text{opp}}}{q_{\text{in}}}$ when $q_{\text{in}} < q_{\text{adj}}$ and $q_{\text{in}} > q_{\text{adj}}$, respectively. In the lattice network, particles regularly visit fracture intersections and streamline routing probabilistically directs more particles to adjacent fractures, causing particle pathlines to more frequently alternate between positive and negative directions. This alternating pattern of positives and negatives cancel, focusing the particle concentration near the initial inlet transverse position (Fig. 4). Hence, particle pathlines are significantly altered by the intersection mixing rule, especially when outlet discharges are similar in magnitude.

The 3D geometry and reduced connectivity of the TPL networks results in transport that is constrained by geometrical and topological network properties. In turn, these features, which are far more complex than the quasi-2D lattice, decreases the impact of the mixing rule relative to the lattice. One such geometrical effect, local flow cells, develop from variations in fracture radii length and orientation, which manifests as elongated tails in solute breakthrough [53]. Additionally, particles remain on fractures for longer distances because they encounter fewer intersections, i.e., solute spreading is structurally constrained. Moreover, fracture aperture is positively correlated to the fracture radius in the TPL networks. By nature of the truncated power-law distributions a small percentage of fractures will therefore have substantially larger permeability and dominate transport due to geometric, topological, and hydrological preference. In combination, these attributes dominate local flow behavior and decrease the impact of the mixing rule.

Furthermore, streamline routing increases the probability of transferring particles to the adjacent fracture in a continuous intersection by a factor of $\frac{q_{\text{adj}}+q_{\text{opp}}}{q_{\text{in}}}$ for $q_{\text{in}} > q_{\text{adj}}$, which is typical in the case of a particle traveling on a preferential flow path. For a particle traveling on such a pathway (which is the majority) in the TPL network, $q_{\mathrm{in}} \approx q_{\mathrm{out}}$ as they lie on the same fracture; $q_{\mathrm{in}} \gg q_{\mathrm{adj}}$ is expected due to the fracture length distribution. This suggests that the probability of a particle changing fractures remains nearly identical ($\frac{q_{\mathrm{adj}}+q_{\mathrm{opp}}}{q_{\mathrm{in}}} \approx 1$) between streamline routing and complete mixing, and the choice of mixing rule is negligible in networks with strong preferential flow pathways, such as the TPL networks considered in this study.

C. Velocity field heterogeneity

Closely coupled with the network structure is the velocity field heterogeneity. In fact, Margolin *et al.* [54] found that increasing the network sparseness has the same effect as increasing the velocity field heterogeneity. As the difference between incoming discharge magnitudes increases, the probability of being routed to the higher magnitude outlet also increases and the impact of the mixing rule decreases. On the lattice, velocity field heterogeneity increases as the variance of the fracture aperture distribution increases. Increasing velocity heterogeneity leads to the development of preferential flow paths in large aperture regions [55], which cause greater channelization of particles and form a subnetwork of fractures that dominate transport. The mean number of times a particle changes fractures decreases with increasing velocity heterogeneity because the probability of transferring from primary fractures decreases. Additionally, the difference in the number of fracture changes between mixing rules also decreases as the velocity field heterogeneity increases. Hence, particle pathlines become more similar and the mixing rule's impact decreases as the velocity heterogeneity increases,which is consistent with the conclusions of Kang *et al.* [10].

In the TPL networks, discharge through a fracture is directly related to the fracture radii, hence the distribution of fracture sizes naturally forms a highly heterogeneous velocity field. The evolution of transverse spreading for both mixing rules looks very similar through TPL networks because the large radii fractures channelize particles and the network geometry drives overall spreading trends. In addition to the velocity field heterogeneity, other factors control transport and reduce the impact of the mixing rule, e.g., network connectivity and geometry [56]. In the context of conservative transport, the higher heterogeneity of the TPL network makes the impact of the mixing rule negligible on spreading metrics, a finding consistent with Park *et al.* [19] who studied conservative transport through 2D DFNs with power-law radii distributions.

D. Implications for reactive transport

The results of this study suggest that the mixing rule has an small impact on common conservative transport metrics (i.e., breakthrough curves, mean-square displacement, and the general distribution of TBPD) in complicated geologic media where the network structure and velocity field are often highly heterogeneous. While these metrics quantify transport behavior at the network scale there are smaller-scale physical and chemical variations in geologic media that are important in the context of reactive transport [57]. In this study we observe that the mixing rule significantly impacts channelization of particles at the fracture scale. Such channelization is important because it drives solute together, enhancing the mixing rate and increasing the probability that two species react [24]. Zou *et al.* [18] showed that the fracture surface roughness increases particle channelization through an intersection, thereby increasing solute mixing at the fracture intersection scale. Similarly, we investigate how channelization due to the intersection mixing rule influences solute mixing, and thus reactions, at the fracture scale.

Consider a system with two reactive species A and B, who undergo the irreversible chemical reaction $A + B \rightarrow C$, such as precipitation of a mineral and two ions [58–61]. The nature of such reaction requires the difference in concentrations of species to be conserved. Denote u as the conserved quantity, where $u = c_A - c_B$ and c_i is the concentration of species i [58]. Consequently, the amount of C that can be precipitated is dependent on the less abundant species between A and B. In geochemical systems described by instantaneous equilibrium reactions, De Simoni *et al.* [58] showed the reaction rate between A and B is a product of a flow driven mixing term $\nabla^T u \nabla u$ and a stoichiometric term. Hence, the mixing rate is directly related to the rate of reaction. The mixing rate is independent of the chemical effects. Since u and particles in DFNWORKS are both conserved quantities and have the same governing equations, we can measure u and therefore the mixing rate. Similar to the TBPD measured in Fig. 9, we also measure the joint y-z breakthrough position distribution at each control plane, i.e., we discretize each control plane into a 2D grid and measure breakthrough concentration in each cell. This enables construction of the 3D position breakthrough field. The position breakthrough field provides the entire u-concentration field that arises after large time in a steady flow, in which u particles are continuously injected. The mixing rate is calculated from this u-concentration field.

The ratio of computed mixing rates using streamline routing and complete mixing is plotted throughout the three-dimensional domain (Fig. 11) for one network realization with a point injection (a) and flux-weighted injection (b). The injection plane is on the front right face and the primary flow direction is directed to the back left face in both figures. The ratio of mixing rates at areas near the inlet where particles have yet to encounter a fraction intersection is 1. After particles pass through fracture intersections, the mixing rule distributes particles differently causing significant local effects in the mixing rates, e.g., notice the yellow streak intersecting the outlet plane where the local mixing rate differs by two orders of magnitudes.

Figure 12 shows the mean normalized mixing rate at each control plane averaged over all realizations for a point injection (a) and flux-weighted injection (b) in the TPL networks. For each realization, the mixing rate is normalized by the maximum mixing rate observed in the streamline routing case. On average, streamline routing elevates the mean mixing rate for both modes of injection. The mixing rate is similar across mixing rules when $x^*/l < 1$, which corresponds to a distance equal to the radii of the largest fracture in the network. After traveling this distance, the mixing rate is noticeably greater when streamline routing is used in the domain.

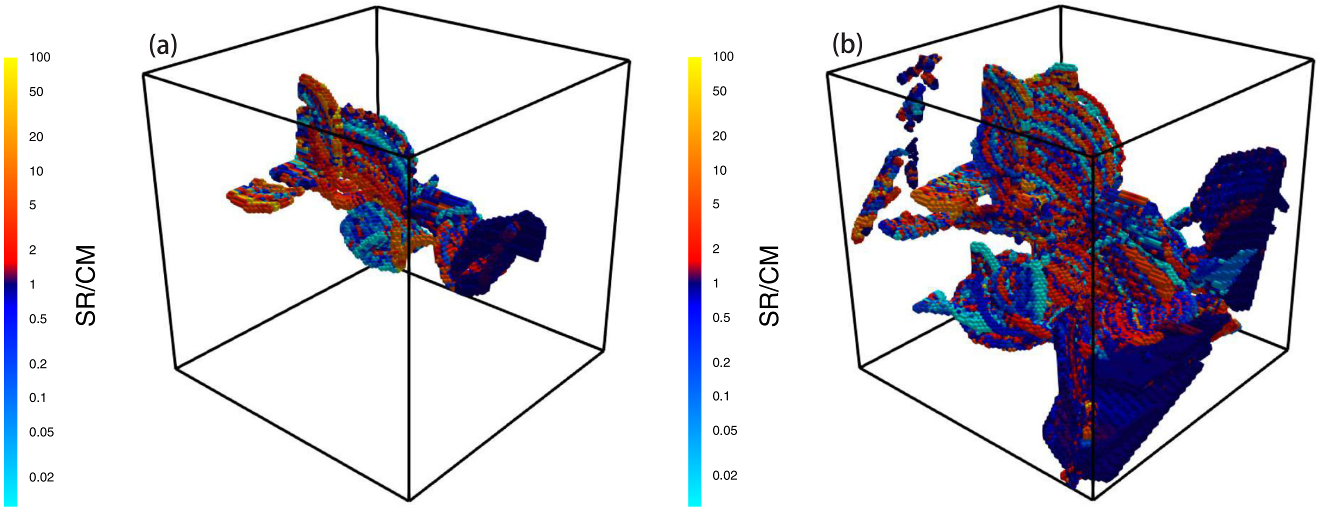

FIG. 11. The ratio streamline routing to complete mixing local mixing ratios is shown for one TPL network realization for a point (a) and flux-weighted (b) initial injection. The front right face is the plane of injection and the back left face is the domain outlet. Colorbars plot the absolute ratio value. Near the inlet plane, the ratio between mixing rules is 1 because transport has yet to encounter fracture intersections. Near the outlet plane, we observe streaks where local mixing rates differ by a factor of 100. Differences in mixing rate occur from differences in channelization of particles due to the mixing rule.

The transverse breakthrough position distributions in the TPL networks display increased channelization of particles on secondary fractures for a streamline routing mixing rule (cf. Fig. 9). These regions of increased channelization are therefore also areas of increased mixing. Hence, it is expected that streamline routing increases the average mixing rate at each control plane. Figure 12 shows that streamline routing increases the mean mixing rate at a distance of approximately equal to the length of the largest fracture radii in the system l^*. Near the particle source, the mixing rule has a smaller impact on channelization because particles have encountered less fracture intersections. At distances exceeding l^* a particle must have encountered at least one fracture intersection and so the mixing rule becomes more important, as fracture intersections enable particles to be channelized to other fractures.

At the fracture scale the local mixing rate can differ by a factor of 100 or greater between the different mixing rules. Such large variation occurs on smaller fractures, which are more sensitive to the mixing rule. Large fractures are less sensitive to the mixing rule because they carry more particles and the probability of switching from them is lower, meaning the concentration gradient is more stable. In systems where solute and the rock boundary react to dissolve and precipitate minerals, a large difference in mixing rate may lead to significant differences in the temporal evolution of transport. Hence implementing the most physically appropriate mixing rule is

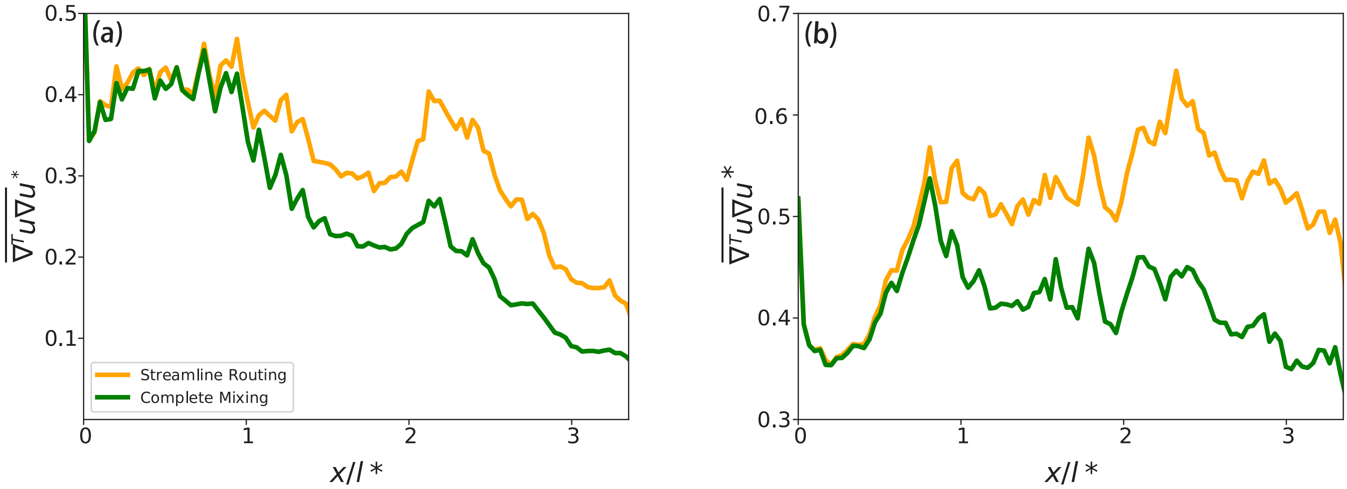

FIG. 12. The mean mixing rate averaged over ten TPL realizations at each control plane is compared for complete mixing (green) and streamline routing (orange) with a point injection (a) and flux-weighted (b) initial injection. In each realization, the mixing rate is normalized by maximum mixing rate observed for streamline routing. Streamline routing increases the mean mixing rate. At distances greater than l^* from the particle source the difference between mixing rules is greater because particles have encountered at least one fracture intersection.

necessary for developing reliable predictive DFN modeling of reactive transport.

Cvetkovic *et al.* [5] simulated sorbing tracers through a 3D DFN. Reactive transport was quantified with a hydrodynamic retention variable β, which is a normalized surface area for diffusion transfer into the rock boundary [62]. They found that streamline routing has a small impact on β compared with complete mixing, but streamline routing does slightly shift β toward higher values. The increased β suggests streamline routing is more reactive. These results are consistent with our observations of increased channelization to secondary fractures under streamline routing, as β increases as aperture size decreases and secondary fractures typically have smaller apertures than primary fractures. β is an averaged parameter over particle trajectories and so the significant local effects observed in this study are not apparent by a slightly increased value. The results of our study suggest that the slight increase in β observed by Cvetkovic *et al.* [62] could be the result of increased channelization of particles to secondary fractures with streamline routing.

VI. REMARKS

We presented a study characterizing the impact of particle behavior at fracture intersections in three-dimensional DFNs on upscaled transport behavior. Mass transfer at fracture intersections in DFN models is represented with two subgrid processes, complete mixing and streamline routing, which are the end member cases of the Pe number, i.e., particle motion through a fracture intersection is governed only by diffusion or advection, respectively. The simulations presented in the previous section indicate that there are scenarios where the choice of mixing rule at fracture intersections have a large impact on transport behavior and other scenarios where the impact is negligible. The magnitude of impact of the mixing rule is determined by the particle initial injection mode, the fracture network structure, and the heterogeneity of the velocity field. The mixing rule's impact increases with a point injection because local effects associated with the fracture of injection control initial particle transport. As the network geometry and velocity field heterogeneity increase, particle channelization to high discharge fractures increase and the impact of the mixing rule on conservative transport at the network scale decreases. In all cases, however, streamline routing increases channelization of mass to secondary fractures, resulting in an increased average mixing rate and local mixing rates that can differ by two orders of magnitude. Therefore, the choice of mixing rule at fracture intersections will influence reactive transport simulations within DFN models. We consider the two end members for intersection mixing rules and our simulations enforce that every intersection prescribes to the same rule. In real geologic media, both advection and diffusion affect mass transfer and a distribution of local fracture intersection Pe exists. Quantifying the impact of these processes warrants future investigation.

ACKNOWLEDGMENTS

T.S. is thankful for support from the Center for Nonlinear Studies at Los Alamos National Laboratory. J.D.H. is thankful for support from the LANL-LDRD Grant No. 20180621ECR. T.S., J.D.H., and G.S. are thankful for support from the LANL-LDRD Grant No. 20170103DR. D.B. and T.S. expresses thanks for financial support via NSF Grants No. EAR-1351625, No. EAR-1446236 and No. CBET-1803989. N.M. is thankful for support from the Used Fuel Disposition Campaign of the United States Department of Energy. This work was funded by the Department of Energy at Los Alamos National Laboratory under Contract No. DE-AC52-06NA25396 through the Laboratory-Directed Research and Development Program. We also are grateful to Shriram Srinivasan for his help generating networks. LA-UR-18-29382

[1] E. Bonnet, O. Bour, N. E. Odling, P. Davy, I. Main, P. Cowie, and B. Berkowitz, Rev. Geophys. **39**, 347 (2001).
[2] S. Pacala and R. Socolow, Science **305**, 968 (2004).
[3] E. Barbier, Renew. Sustain. Energy Rev. **6**, 3 (2002).
[4] J. Hyman, J. Jiménez-Martínez, H. Viswanathan, J. Carey, M. Porter, E. Rougier, S. Karra, Q. Kang, L. Frash, L. Chen *et al.*, Philos. Trans. R. Soc. A **374**, 20150426 (2016).
[5] V. Cvetkovic, S. Painter, N. Outters, and J. Selroos, Water Resour. Res. **40**, W02404 (2004).
[6] J. Hyman and J. Jiménez-Martínez, Water Resour. Res. **54**, 3243 (2018).
[7] J.-R. de Dreuzy, Y. Méheust, and G. Pichot, J. Geophys. Res.: Solid Earth **117**, B11207 (2012).
[8] N. Makedonska, J. D. Hyman, S. Karra, S. L. Painter, C. W. Gable, and H. S. Viswanathan, Adv. Water Resour. **94**, 486 (2016).
[9] J. Johnson, S. Brown, and H. Stockman, J. Geophys. Res.: Solid Earth **111**, B12206 (2006).
[10] P. K. Kang, M. Dentz, T. Le Borgne, and R. Juanes, Phys. Rev. E **92**, 022148 (2015).
[11] R. J. Krizek, R. M. Karadi, and E. Socias, in *Proceedings of the International Society of Rock Mechanics Symposium on Percolation Through Fissured Rock, Stuttgart, Germany* (Deutsche Gesellschaft für Erd- und Grundbau, 1972).
[12] C. R. Wilson and P. Witherspoon, Water Resour. Res. **12**, 102 (1976).
[13] L. Hull and K. Koslow, Water Resour. Res. **22**, 1731 (1986).
[14] J. W. Robinson and J. E. Gale, Groundwater **28**, 25 (1990).
[15] B. Berkowitz, C. Naumann, and L. Smith, Water Resour. Res. **30**, 1765 (1994).
[16] H. W. Stockman, C. Li, and J. L. Wilson, Geophys. Res. Lett. **24**, 1515 (1997).
[17] V. Mourzenko, F. Yousefian, B. Kolbah, J.-F. Thovert, and P. Adler, Water Resour. Res. **38**, 1000 (2002).
[18] L. Zou, L. Jing, and V. Cvetkovic, Adv. Water Resour. **107**, 1 (2017).
[19] Y. J. Park, J. de Dreuzy, K. K. Lee, and B. Berkowitz, Water Resour. Res. **37**, 2493 (2001).
[20] J. Küpper, F. Schwartz, and P. Steffler, J. Contam. Hydrol. **18**, 33 (1995).

[21] Y. J. Park, K. K. Lee, and B. Berkowitz, Water Resour. Res. **37**, 909 (2001).
[22] J. D. Hyman, S. Karra, N. Makedonska, C. W. Gable, S. L. Painter, and H. S. Viswanathan, Comput. Geosci. **84**, 10 (2015).
[23] T. Aquino and D. Bolster, Transp. Porous Media **119**, 391 (2017).
[24] E. E. Wright, D. H. Richter, and D. Bolster, Phys. Rev. Fluids **2**, 114501 (2017).
[25] S. P. Neuman, Hydrogeol. J. **13**, 124 (2005).
[26] P. Lichtner, G. Hammond, C. Lu, S. Karra, G. Bisht, B. Andre, R. Mills, and J. Kumar, PFLOTRAN User Manual: A Massively Parallel Reactive Flow and Transport Model for Describing Surface and Subsurface Processes, Los Alamos National Laboratory Technical Report No. LA-UR-15-20403, 2015 (unpublished).
[27] M.-C. Cacas, E. Ledoux, G. de Marsily, B. Tillie, A. Barbreau, E. Durand, B. Feuga, and P. Peaudecerf, Water Resour. Res. **26**, 479 (1990).
[28] J.-R. de Dreuzy, C. Darcel, P. Davy, and O. Bour, Water Resour. Res. **40**, W01502 (2004).
[29] I. I. Bogdanov, V. V. Mourzenko, J.-F. Thovert, and P. M. Adler, Phys. Rev. E **76**, 036309 (2007).
[30] J. D. Hyman, S. L. Painter, H. Viswanathan, N. Makedonska, and S. Karra, Water Resour. Res. **51**, 7289 (2015).
[31] J. D. Hyman, G. Aldrich, H. Viswanathan, N. Makedonska, and S. Karra, Water Resour. Res. **52**, 6472 (2016).
[32] S. Karra, N. Makedonska, H. Viswanathan, S. Painter, and J. Hyman, Water Resour. Res. **51**, 8646 (2015).
[33] J. D. Hyman, C. W. Gable, S. L. Painter, and N. Makedonska, SIAM J. Sci. Comput. **36**, A1871 (2014).
[34] LaGriT, Los Alamos Grid Toolbox (LaGriT), Los Alamos National Laboratory, http://lagrit.lanl.gov (2013).
[35] N. Makedonska, S. L. Painter, Q. M. Bui, C. W. Gable, and S. Karra, Comput. Geosci. **19**, 1123 (2015).
[36] S. Painter, C. Gable, and S. Kelkar, Comput. Geosci. **16**, 1125 (2012).
[37] A. Kreft and A. Zuber, Chem. Eng. Sci. **33**, 1471 (1978).
[38] A. Frampton and V. Cvetkovic, Water Resour. Res. **47**, W02506 (2011).
[39] J. Philip, Water Resour. Res. **24**, 239 (1988).
[40] X. Sanchez-Vila, A. Guadagnini, and J. Carrera, Rev. Geophys. **44**, RG3002 (2006).
[41] J.-R. de Dreuzy, P. Davy, and O. Bour, Water Resour. Res. **37**, 2079 (2001).
[42] J. Long and D. M. Billaux, Water Resour. Res. **23**, 1201 (1987).
[43] O. Bour and P. Davy, Water Resour. Res. **33**, 1567 (1997).
[44] P. Davy, J. Geophys. Res.: Solid Earth **98**, 12141 (1993).
[45] N. E. Odling, J. Struct. Geol. **19**, 1257 (1997).
[46] G. Ouillon, C. Castaing, and D. Sornette, J. Geophys. Res.: Solid Earth **101**, 5477 (1996).
[47] J.-R. de Dreuzy, P. Davy, and O. Bour, Water Resour. Res. **38**, 1276 (2002).
[48] A. Frampton and V. Cvetkovic, Water Resour. Res. **46**, W11502 (2010).
[49] S. Joyce, L. Hartley, D. Applegate, J. Hoek, and P. Jackson, Hydrogeol. J. **22**, 1233 (2014).
[50] T. P. Wellman, A. M. Shapiro, and M. C. Hill, Water Resour. Res. **45**, W01416 (2009).
[51] J.-R. de Dreuzy, P. Davy, and O. Bour, Phys. Rev. E **62**, 5948 (2000).
[52] M. Dentz, P. K. Kang, A. Comolli, T. Le Borgne, and D. R. Lester, Phys. Rev. Fluids **1**, 074004 (2016).
[53] Y. Park, K. Lee, G. Kosakowski, and B. Berkowitz, Water Resour. Res. **39**, 1215 (2003).
[54] G. Margolin, B. Berkowitz, and H. Scher, Water Resour. Res. **34**, 2103 (1998).
[55] S. Brown, A. Caprihan, and R. Hardy, J. Geophys. Res.: Solid Earth **103**, 5125 (1998).
[56] P. M. Adler and J.-F. Thovert, *Fractures and Fracture Networks* (Springer Science & Business Media, Berlin, 1999), Vol. 15.
[57] M. Dentz, T. Le Borgne, A. Englert, and B. Bijeljic, J. Contam. Hydrol. **120**, 1 (2011).
[58] M. D. Simoni, J. Carrera, X. Sánchez-Vila, and A. Guadagnini, Water Resour. Res. **41**, W11410 (2005).
[59] M. De Simoni, X. Sanchez-Vila, J. Carrera, and M. Saaltink, Water Resour. Res. **43**, W07419 (2007).
[60] L. D. Donado, X. Sanchez-Vila, M. Dentz, J. Carrera, and D. Bolster, Water Resour. Res. **45**, W11402 (2009).
[61] X. Fu, L. Cueto-Felgueroso, D. Bolster, and R. Juanes, J. Fluid Mech. **764**, 296 (2015).
[62] V. Cvetkovic, J. Selroos, and H. Cheng, J. Fluid Mech. **378**, 335 (1999).